Brushless traction PM machines using commercial drive technology, part II: Comparative study of the motor configurations

Brushless Traction PM Machines Using Commercial Drive Technology, Part II: Comparative Study of the Motor Configurations

Evgeny V. Kazmin, Elena A. Lomonova, Johannes J.H. Paulides
Department of Electrical Engineering, Eindhoven University of Technology, The Netherlands
Email: e.lomonova@tue.nl

***Abstract* – In Part II a comparative analysis of the different brushless PM motor configurations, including exterior and interior rotor arrangements, salient and non-salient surface-mounted PM rotors, concentrated and distributed armature windings is presented. The comparative study is based on the developed design methodology given in the Part I of this paper. These motor configurations are investigated to be exploited for the particular automotive application – in-wheel hub traction motor of 80 kW, 1000 rpm base speed and constant power speed range of 4.5:1. It is shown that the interior surface-mounted non-salient PM motor with the concentrated winding is the most appropriate machine type for the considered application.**

I. INTRODUCTION

Selection of the most appropriate motor type for a traction application is often not trivial task. Such design factors as a steel saturation, cooling capabilities of a cooler, wide constant power speed range and geometry constraints can limit a number of possible motor types and configurations. As it is well-known, synchronous (both, AC and DC) brushless PM machines have a highest power density among the traction motors of induction, brushed DC and switched-reluctance types. This feature makes the PM machines more attractive for hybrid electric vehicle application.

In the Part I of this paper the studied candidates of the PM machines are presented. The considered rotor configurations with the SPM and IPM types in case of exterior arrangement are shown in Fig. 1. In order to minimize rotor eddy current losses at higher speeds in the both configurations back-irons are laminated. As the permeability of iron-neodymium-boron magnets is close to the permeability of air, the SPM motor is non-salient and operates on the magnet alignment torque. Due to large equivalent airgap, higher level of magnetic flux density could be selected in that configuration without causing of significant saturation in the rotor. In the IPM design the magnets are placed in special rotor opened or closed (by saturation bridges) slots, as shown in Fig. 1(b). The airgap under the magnets and, so-called, *q*-ribs (rotor teeth), is different that makes the IPM motor as a salient one. Thus, the IPM motor operates on reluctance torque and magnet alignment torque as well, that leads, in general, to the better performance in wide range of CPSR applications [1]. Higher level of torque ripples and higher rotor core losses are the main drawbacks of the IPM design [2].

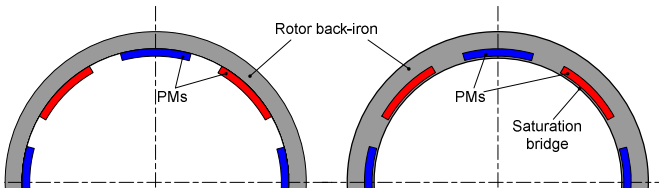

Fig. 1. Considered exterior rotor configurations: (a) – SPM rotor and (b) – IPM rotor

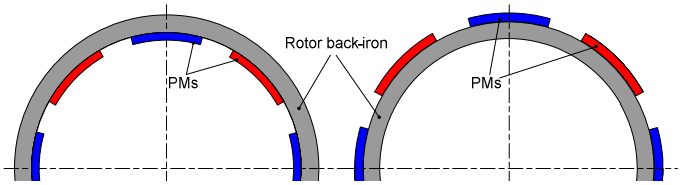

Fig. 2: Considered rotor configurations with SPM: (a) – exterior rotor and (b) – interior rotor

The different SPM rotor arrangements with respect to the stator are shown in Fig. 2. Main advantage of the exterior rotor is that the motor could be designed with larger airgap diameter, since the magnet height is usually sufficiently less than a height of the stator slot. As it is well-known, the output power of the electrical machine is proportional to the airgap diameter squared, so it is favorable to have the airgap diameter as large as possible.

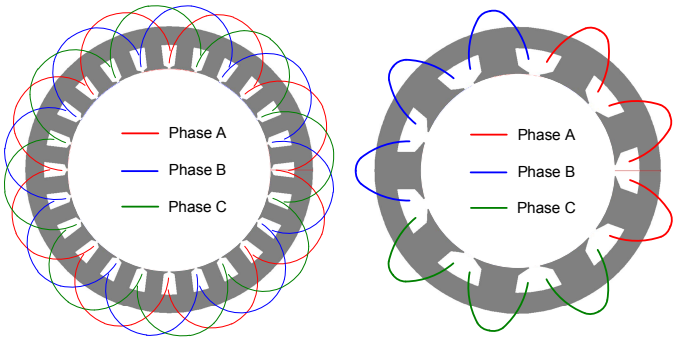

(a) (b)

Fig. 3: Armature winding types for an interior rotor machine: a) – distributed winding; b) – concentrated winding

Another item of the motor configuration to be observed is an armature winding type. Three phase double or single layer distributed lap winding and three phase double layer concentrated winding have been considered. The sketches of these windings are shown in Fig. 3.

In order to find optimal machine variant it is necessary to provide conceptual electromagnetic, thermal and ventilation (or hydraulic) analyses for all possible PM motor types. The comparative analysis of performances of the different PM motor is the subject of this paper.

II. External or Internal Rotor

In this section considerations of the rotor arrangement are discussed. It is necessary to check that exterior rotor machine could be effectively cooled by the given cooling system. As it is mentioned in the Part I of this paper, in case of the exterior rotor configuration a water jacket is placed in the stator hub (instead of the stator housing), where cooled surface has low area and, therefore, low cooling capability.

In the Part I the basic geometry data and performance of the designed surface-mounted PM motor with internal rotor (IR) and concentrated winding are presented. Some data of this machine, which is required for the current section, is given in Table I. Some symbols in the table contain an index "*I*", which shows that they correspond only to the internal rotor machine and are different in the case of external rotor machine. The values, which symbols are not containing the "*I*", will be the same for the both rotor arrangements.

It is possible to apply these results for external rotor (ER) machine with the same armature winding, rotor type and the same level of the output power. The airgap length, magnet height, power factor, rotor back iron height (h_{yrE}=h_{yrI}) and armature current density could be assumed to be equal to the same data of IR machine.

TABLE I
THE SPM MOTOR DATA WITH INTERNAL ROTOR STRUCTURE AND CONCENTRATED WINDING

Description	Symbol	Value	Unit
Stator outer diameter	D_{ODI}	0.5013	m
Stack length	l_{1I}	0.1	m
Rotor back iron height	h_{yrI}	0.0368	m
Magnet height	h_m	0.0075	m
Stator bore diameter	D_{1I}	0.338	m
Stator slot depth	h_s	0.045	m
Coil height (at the slot middle)	h_{cI}	0.0299	m
Slot opening height	h_{so}	0.003	m
Airgap	δ	0.001	m
Electrical loading (rms)	A_{1I}	56000	A/m
Current density	J_I	$5\cdot10^6$	A/m^2
End winding length per side	l_{ew}	0.045	mm
Armature copper losses	P_{cuI}	1458	W
Slot width to slot pitch ratio	k_{bs_tz}	0.45	-

Stack length of the ER machine should be decreased by a rim thickness. The rim thickness could be assumed equal to a half of rotor back iron height. So, stator stack length is:

$$l_{1E} = l_{1I} - \frac{h_{yrE}}{2} = 0.1 - \frac{0.0368}{2} = 0.0816 \quad m. \tag{1}$$

Stator bore diameter of the ER machine follows as:

$$D_{1E} = D_{ODI} - 2\cdot(h_m + h_{yrE} + \delta) = 0.5013 - 2\cdot(0.0075 + 0.0368 + 0.001) = 0.4107 \quad m. \tag{2}$$

Because of the ER machine has larger airgap diameter the electrical loading could be decreased. Using equation for a machine constant it is possible to define the electrical loading. The machine constant is formulated as [3]:

$$C_A = \frac{D_1^2 \cdot l_1 \cdot n}{P/\cos\varphi} = \frac{2}{\pi \cdot C_w \cdot A_1 \cdot B_\delta}. \tag{3}$$

where C_w=$\alpha_\delta k_w k_B/k_E$ – geometry and winding data coefficient; α_δ – pole overlap factor; k_w – winding factor; k_B – back-emf waveform factor; k_E – back-emf magnitude factor; B_δ – airgap peak flux density [T].

Assuming that C_w and B_δ are the same in the both ER and IR machine designs, electrical loading of the ER machine yields:

$$A_{1E} = \left(\frac{D_{1I}}{D_{1E}}\right)^2 \cdot \frac{l_{1I}}{l_{1E}} \cdot A_{1I} = \left(\frac{0.338}{0.4107}\right)^2 \cdot \frac{0.1}{0.0816} \cdot 56000 = 46500 \quad \frac{A}{m}. \tag{4}$$

The temperature rise between stator armature winding and water jacket channel could be defined as [4]:

$$\theta_\alpha = \frac{P_h}{\alpha \cdot S_{col}}, \tag{5}$$

where P_h – heat fluid, which goes from the stator to the water jacket [W]; α – heat transfer factor between stator back iron and water jacket [W/(m^2°C)]; S_{col} – area of the cooled surface of the stator [m^2].

At base speed a fundamental frequency is equal to 60 Hz and armature winding losses are the largest component of the total motor losses. Furthermore, it could be assumed that almost all armature copper losses are taken away through water jacket. Thus, the heat fluid P_h is approximately equal to

P_{cu}, which is defined by (6):

$$P_{cu} = A_1 \cdot J_1 \cdot k_{AC/DC} \cdot \rho_{cu\_OT} \cdot D_1 \cdot (l_1 + l_{ew}) \cdot \pi, \quad (6)$$

where $k_{AC/DC}$=1.05 – AC/DC resistance ratio; ρ_{cu_OT}=2.17·10^{-8} – copper resistance at operating temperature [Ohm ·m].

Assuming that the end winding length of the ER machine is approximately equal to the same value of the IR machine, the armature copper losses of the ER motor could be found out from (6) as follows:

$$P_{cuE} = 465 \cdot 10^2 \cdot 5 \cdot 10^6 \cdot 1.05 \cdot 2.17 \cdot 10^{-8} \cdot 0.4107 \cdot (0.0816 + 0.045) \cdot \pi = 865 \quad W. \quad (7)$$

Now it is possible to define required cooled surface of the ER machine. In order to have the same armature winding temperature rise the following equation should be satisfied (according to (5)):

$$\frac{P_{cuI}}{\alpha_I \cdot S_{colI}} = \frac{P_{cuE}}{\alpha_E \cdot S_{colE}}. \quad (8)$$

If coolant speed in water jacket channels and cross-sectional dimensions of the channels are the same in both designs, then the heat transfer factors α_I and α_E are approximately equal to each other [4]. By using equation (8) the cooled surface of the ER motor could be defined as following:

$$S_{colE} \geq \frac{P_{cuE}}{P_{cuI}} \cdot S_{colI} = \frac{865}{1458} \cdot S_{colI} \cong 0.6 \cdot S_{colI}. \quad (9)$$

In fact, the cooled surface is proportional to the outer (inner for ER motor) diameter of the stator. It could be written the following expression:

$$\frac{S_{colE}}{S_{colI}} = \frac{D_{ODE}}{D_{ODI}}, \quad (10)$$

where D_{ODE} – inner diameter of the ER machine:

$$D_{ODE} = D_{1E} - 2 \cdot (\delta + h_{ysE} + h_{sE}), \quad (11)$$

where h_{ysE} – stator back iron height [m], it is assumed that h_{ysE}=h_{yrI}; h_{sE} – slot depth.

Stator slot depth of the ER motor is normally larger than stator slot depth of the IR machine. The sketches of stator slots of an ER and IR machine types are shown in Fig. 4.

The h_{sE} is defined as (Fig. 4 (b)):

$$h_{sE} = h_{cE} + h_w + h_{so}, \quad (12)$$

where h_{cE} – coil height [m]. It is necessary now to define the h_{cE}.

An area of the ER machine slot that is filled with the coils is expressed as (Fig. 4 (b)):

$$A'_{slE} = \frac{1}{2} \cdot (b_{s2E} + b_{s3E}) \cdot h_{cE}. \quad (13)$$

On the other hand this area could be defined as [m^2]:

$$A'_{slE} = \frac{A_{1E} \cdot t_{z2E}}{J_1 \cdot k_f}, \quad (14)$$

where t_{z2E} – slot pitch at the level of the coil top [m]. The t_{z2E} is given by:

$$t_{z2E} = \frac{\pi \cdot [D_{1E} - 2 \cdot (h_w + h_{so})]}{Z} = \frac{\pi \cdot [0.4107 - 2 \cdot (0.012 + 0.003)]}{9} = 0.1329 \quad m. \quad (15)$$

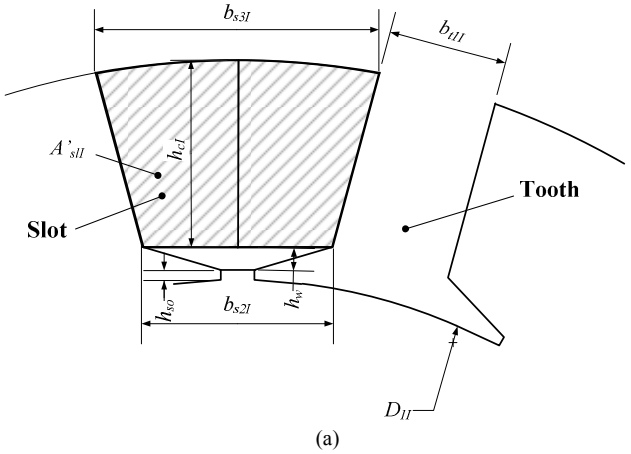

(a)

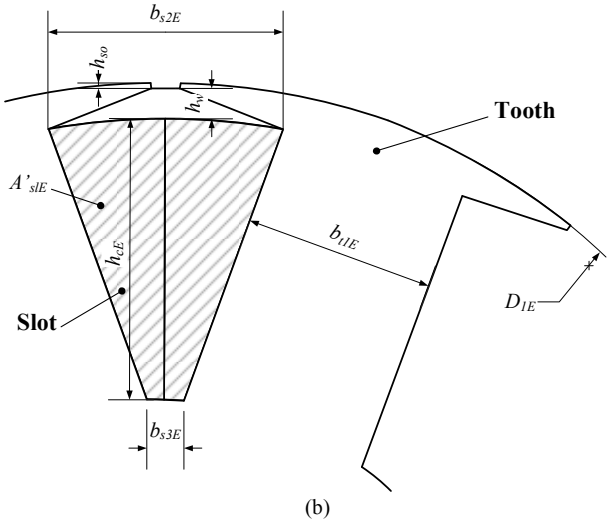

(b)

Fig. 4: The sketches of the stator slot and tooth:
(a) – internal rotor machine; (b) – external rotor machine

The unknown slot width b_{s3E} could be defined using (7) from the Part I of this paper. The stator tooth width is equal to:

$$b_{t1E} = t_{z1E} - b_{s1E} = t_{z1E} \cdot (1 - k_{bs\_tz}) = \frac{\pi \cdot D_{1E} \cdot (1 - k_{bs\_tz})}{Z} = \frac{\pi \cdot 0.4107 \cdot (1 - 0.45)}{9} = 0.0788 \quad m. \quad (16)$$

In (16) the slot width to slot pitch ratio k_{bs_tz} is taken equal to 0.45, as for the designed IR machine (Table I).

Stator slot width at the level of the coil top b_{s2E} yields (Fig. 4 (b)):

$$b_{s2E} = \frac{\pi \cdot (D_{1E} - 2 \cdot (h_w + h_{so}))}{Z} - b_{t1E} = \frac{\pi \cdot (0.4107 - 2 \cdot (0.012 + 0.003))}{9} - 0.0788 = 0.054 \quad m. \quad (17)$$

Omitting simple calculations one can define that b_{s3E} = 0.0163 m.

From (13) and (14) the coil height yields:

$$h_{cE} = \frac{2 A_{1E} \cdot t_{z2E}}{J_1 \cdot k_f (b_{s2E} + b_{s3E})} = \frac{2 \cdot 46500 \cdot 0.1329}{5 \cdot 10^6 \cdot 0.65 \cdot (0.054 + 0.0163)} = 0.0541 \quad m. \quad (18)$$

The slot depth is defined as (according to (12)):

$$h_{sE} = 0.0541 + 0.012 + 0.003 = 0.0691 \quad m. \tag{19}$$

Once the stator slot depth of the ER machine is defined, now it is possible to calculate the ratio of the cooled surfaces as given in (10) and (11):

$$\frac{S_{colE}}{S_{colI}} = \frac{D_{1E} - 2\cdot(\delta + h_{ysE} + h_{sE})}{D_{OD1}} = \frac{0.4107 - 2\cdot(0.001 + 0.0368 + 0.0691)}{0.5013} = \frac{0.1989}{0.5013} = 0.39. \tag{20}$$

Equation (20) shows that the cooled surface of the ER motor is only 39% of cooled surface of the IR motor. From equation (9) it is seen that required cooled surface should not be less than 60%, therefore, electrical load and respectively output power of the ER machine have to be reduced by 60% - 39% = 21% in order to have the same armature copper temperature. Thus, the ER machine is not suitable motor type for the given application.

III. SPM OR IPM DESIGNS

As it is mentioned in the section I, the IPM motor has the saliency along *q*-axis and, owing to that circumstance, can has more output power as at base speed, so at other field-weakening (FW) operation points. However, the high performance of the IPM machines is significantly influenced by a steel saturation. Especially it occurs in highly rated machines with high level of the airgap flux density. At base speed an armature reaction flux is oriented mostly along *q*-axis, where the lowest airgap exists, and peak value of the flux density is increased as much as lower airgap height. Since a permanent magnet flux is directed along *d*-axis, one can assume that it does not influence on the *q*-axis resultant flux.

In the SPM motor the *q*-axis airgap flux density could be significantly lower than in the IPM motor even at higher level of the armature reaction magnetomotive force (MMF), because of the larger equivalent airgap height. This equivalent airgap is mostly formed by the permanent magnets, which have relative permeability near of the unity.

Due to small airgap height the armature reaction flux is almost not decayed and penetrated into the rotor teeth with approximately the same magnitude as it has at stator bore surface. Thus, it could be assumed the following:

$$B_{tr} = B^{I}_{aqm}, \tag{21}$$

where B_{tr} – peak flux density in the rotor tooth due to *q*-axis armature reaction flux, B^{I}_{aqm} – peak airgap flux density of the *q*-axis armature reaction flux of the IPM machine [T].

If the B_{tr} is higher than saturation flux density of the rotor steel, the rotor teeth becomes as an air in magnetic terms, and saliency of the IPM motor will be eliminated and output power will decreased.

The SPM and IPM machines geometry sketches, the qualitative waveforms of the *q*-axis reaction MMFs and airgap flux densities caused by these MMFs are shown in Fig. 5. The geometry sketches are presented with eliminating a curvature of the real machines.

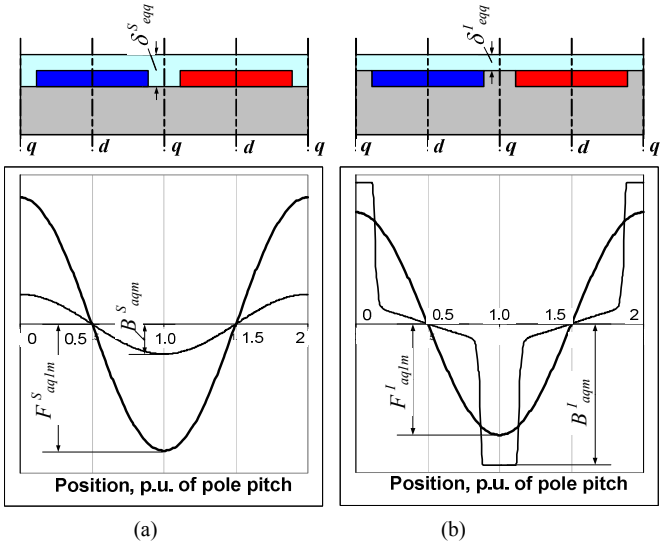

(a) (b)

Fig. 5: The sketches of the two poles rotor geometries, armature q-axis MMF and airgap flux density waveforms: (a) – for SPM machine; (b) – for IPM machine

The *q*-axis MMFs in both machine designs are caused by the *q*-axis component of the armature winding current and have strictly sinusoidal waveform, as shown in Fig. 4. The airgap flux density in the SPM motor repeats the waveform of the MMF due to uniform airgap. It should be noted that in Fig. 4 and for further analysis the relative permeability of the permanent magnets is assumed to be equal to unity. In contrast to SPM machine the *q*-axis airgap flux density of the IPM machine notably differs from the corresponding MMF waveform. It has trapezoidal shape with maximum magnitude under rotor teeth. The peak flux density of the IPM machine, B^{I}_{aqm}, is notably higher than the respective value of the SPM machine, B^{S}_{aqm}. The main purpose of this section is to show how high the B^{I}_{aqm}-value will be in comparison with a known value of the B^{S}_{aqm}, which could be derived from the data of the already designed SPM motor (Part I of this paper).

It is possible to assess the B^{I}_{aqm} and, respectively, maximum flux density in the rotor tooth, by extending the data of the SPM motor. For that purpose the IPM motor with the same stator geometry and dimensions of the magnets should be considered. The difference between the rotors of the SPM and IPM designs is only that the inter-polar space of the IPM machine is filled by the laminations (as rotor back-iron).

The *q*-axis peak airgap flux density caused by the armature reaction flux is defined as [5]:

$$B_{aqm} = \mu_0 \cdot \frac{F_{aq1m}}{\delta_{eqq}}, \tag{22}$$

where $\mu_0 = 4\pi 10^{-7}$ [H/m] – magnetic constant; F_{aq1m} – fundamental harmonic amplitude of the *q*-axis armature MMF [A t]; δ_{eqq} – *q*-axis equivalent airgap [m].

The F_{aq1m} is expressed as:

$$F_{aq1m} = \frac{m_1 \cdot \sqrt{2}}{\pi} \cdot \frac{w_1 \cdot k_w}{6p} \cdot I_1 \cdot \cos\gamma. \tag{23}$$

where m_1 – a number of phases; w_1 – a number of series turns in phase; k_w – winding factor; p – a number of pole pairs, I_1 – phase current A (rms); γ – torque control angle [rad]

(angle between phasors of armature current and back-emf).

The phase current, I_1, could be formulated as follows:

$$I_1 = \frac{\pi \cdot D_1 \cdot A_1}{6 w_1}. \quad (24)$$

Substituting (24) into (23) the q-axis MMF yields:

$$F_{aq1m} = \frac{m_1 \cdot \sqrt{2} \cdot k_w}{\pi} \cdot D_1 \cdot A_1 \cdot \cos\gamma. \quad (25)$$

Using (24) the q-axis MMFs of the SPM and IPM machines could be written as the following:

$$F^S_{aq1m} = \frac{m_1 \cdot \sqrt{2} \cdot k_w}{\pi} \cdot D_1 \cdot A^S_1 \cdot \cos\gamma^S,$$
$$F^I_{aq1m} = \frac{m_1 \cdot \sqrt{2} \cdot k_w}{\pi} \cdot D_1 \cdot A^I_1 \cdot \cos\gamma^I, \quad (26)$$

where A^S_1 and A^I_1 – electrical loadings of the SPM and IPM machines, respectively; γ^S and γ^I – armature current angles of the considered machines. The values in (26), which do not have upper indexes 'S' and 'I ', are the same, as it is mentioned that geometry data of both machines is identical.

Let us divide the second equation in (26) by the first one:

$$\frac{F^I_{aq1m}}{F^S_{aq1m}} = \frac{A^I_1 \cdot \cos\gamma^I}{A^S_1 \cdot \cos\gamma^S}. \quad (27)$$

At the base speed current angle, providing the highest torque, of the SPM machine, γ^S, is equal to zero [6]. Then (27) could be rewritten as follows:

$$\frac{F^I_{aq1m}}{F^S_{aq1m}} = \frac{A^I_1 \cdot \cos\gamma^I}{A^S_1}. \quad (28)$$

By expressing the F_{aq1m} from (22) and substituting into (28) for each motor design one can express:

$$\frac{B^I_{aq1m} \cdot \delta^I_{eqq}}{B^S_{aq1m} \cdot \delta^S_{eqq}} = \frac{A^I_1 \cdot \cos\gamma^I}{A^S_1}, \quad (29)$$

where δ^I_{eqq} and δ^S_{eqq} – equivalent q-axis airgaps of the IPM and SPM machines, respectively.

The equivalent airgap of the IPM machine is defined as:

$$\delta^I_{eqq} = \delta \cdot k_{\delta 1}. \quad (30)$$

The equivalent airgap of the SPM machine is defined as:

$$\delta^S_{eqq} = (\delta + h_m) \cdot k_{\delta 1}. \quad (31)$$

In (31) the assumption is made that relative permeability of the magnets is equal to unity. Substituting (30) and (31) into (29) it could be re-written:

$$\frac{B^I_{aq1m}}{B^S_{aq1m}} = \frac{h_m + \delta}{\delta} \cdot \frac{A^I_1 \cdot \cos\gamma^I}{A^S_1}. \quad (32)$$

Since $h_m >> \delta$, as shown in Table I in the Part I of this paper, (32) could be rewritten as follows:

$$\frac{B^I_{aq1m}}{B^S_{aq1m}} \approx \frac{h_m}{\delta} \cdot \frac{A^I_1 \cdot \cos\gamma^I}{A^S_1}. \quad (33)$$

Using (33) the flux density B^I_{aq1m} yields:

$$B^I_{aq1m} \approx B^S_{aq1m} \cdot \frac{h_m}{\delta} \cdot \frac{A^I_1 \cdot \cos\gamma^I}{A^S_1}. \quad (34)$$

As it is seen from equation (34) the q-axis airgap flux density of the IPM machine is h_m/δ times larger than the corresponding flux density of the SPM machine. It is observed under condition of $A^S_1 = A^I_1 \cos\gamma^I$. In fact, at base speed the current angle of the IPM machine $\gamma^I > 0$ [6], therefore, $\cos\gamma^I < 1$; and, on a second hand, A^I_1 could be lower than A^S_1. The last circumstance is described by the fact that the IPM machine can have higher output power and the electrical loading could be decreased in order to keep output power at same required level. An assessment of the A^I_1 and γ^I is given further.

The flux density B^S_{aq1m} could be found from the equations (22), (25) and by using the SPM motor data, which is given in Table I and Table II in the Part I of this paper as follows:

$$B^S_{aq1m} = \frac{\mu_0 \cdot m_1 \cdot \sqrt{2}}{\pi} \cdot \frac{w_1 \cdot k_w}{p} \cdot I_1^2 \cdot \frac{1}{(h_m + \delta) \cdot k_{\delta 1}} =$$
$$\frac{4\pi \cdot 10^{-7} \cdot 3 \cdot \sqrt{2}}{\pi} \cdot \frac{78 \cdot 0.945}{4} \cdot 138.3^2 \cdot$$
$$\frac{1}{(0.0075 + 0.001) \cdot 1.399} = 0.334 \quad T. \quad (35)$$

Using the developed analytical model (Part I of this paper) the IPM motor has been designed. The stator geometry and winding data of this machine is equal to the same data of the designed SPM motor. As it is mentioned before, the only difference between considering SPM and IPM machines is that the rotor inter-polar space of the IPM motor is filled by the laminations. The rotor cross sections of both machines are shown in Fig. 6. Below in Table II the comparison of key parameters of the SPM and IPM machines are presented.

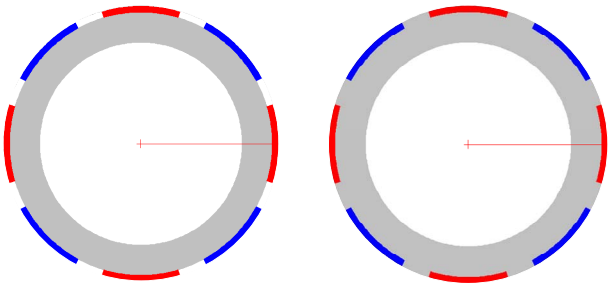

(a) (b)

Fig. 6: Rotor cross sections of the (a) SPM and (b) IPM machines

TABLE II
THE KEY DISTINCTIVE PARAMETERS OF THE DESIGNED MACHINES

Description	Symbol	SPM	IPM	Unit
Electrical loading (rms)	A_1	56000	53900	A/m
Saliency ratio	ξ	1	1.481	-
Current angle	γ	0	22.0	^{o}

Electromagnetic loading, A^I_1, of the IPM machine is selected in order to achieve the same output power at base speed as in the SPM machine. The steel saturation is not taken into account, therefore, the saliency ratio of the IPM motor, $\xi^I = 1.481$, is the maximum possible saliency ratio that could be achieved from the considered IPM rotor type, and a product of $A^I_1 \cdot \cos\gamma^I$ is the lowest.

Substituting (21) into (34) the rotor teeth peak flux density could be estimated as follows:

$$B^I_{aq1m} \approx 0.334 \cdot \frac{0.0075}{0.001} \cdot \frac{53900 \cdot \cos 22}{56000} = 2.234 \quad T. \quad (36)$$

Since the rotor teeth flux density $B_{tr} = 2.234$ T (i.e. is in the zone of the deep steel saturation), it could be assumed that the saliency ratio of the considered IPM motor is near the unity and the motor will have a performance of a SPM machine. In

order to check this conclusion the steady-state FEA of the base speed operation mode has been conducted. Vector sum of flux density and flux lines for arbitrary instant of time are shown in Fig. 7. The distribution of the normal component of the air flux density along rotor outer surface at the same instant of time is presented in Fig. 8. The airgap flux density is given for two rotor poles (90 ^{o}).

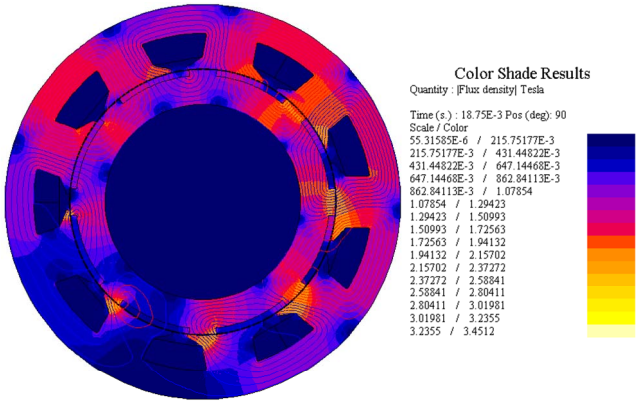

Fig. 7: Colour map of flux density vector sum and 2D flux lines

As it could be seen in Fig. 7 and Fig. 8 the rotor teeth flux density reaches the peak value near 2 T. This calculated flux density differs from assumed 2.234 T. That difference could be described by the steel saturation and real airgap flux distribution, including the magnet fluxes, which have not been taken into account in analytical analysis. The main motor performance characteristics, which are liable to the rotor steel saturation, are given in Table III. Due to the almost saturated rotor teeth the saliency ratio of the motor is approximately equal to unity and output power is reduced. Thus, with the considered type of an IPM machine it is not possible to achieve better performance than in designed SPM motor and, therefore, it is not worth to use it in the given application.

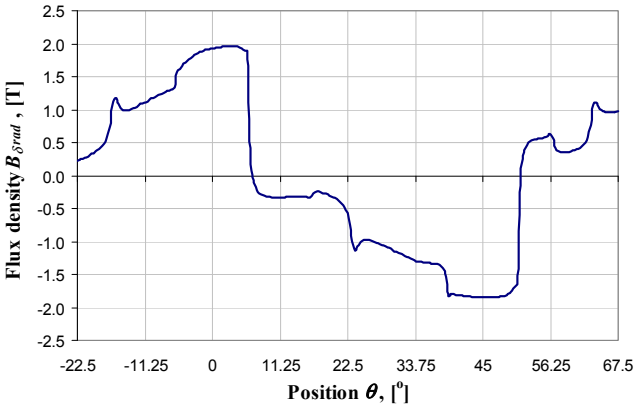

Fig. 8: Radial component of the airgap flux density along outer rotor surface

TABLE III
IMPACT OF THE ROTOR TEETH SATURATION ON THE IPM MOTOR PARAMETERS

Description	Symbol	Unit	Analytical model (without steel saturation)	FEA (with steel saturation)
q-axis armature synchronous reactance	X_q	Ohm	1.4776	1.2536
d-axis armature synchronous reactance	X_d	Ohm	0.9979	1.2200
Saliency ratio	ξ	-	1.481	1.027
Back-emf (rms)	E_q	V	138.9	140.1
Phase voltage (rms)	V_1	V	224.4	191.1
Output power	P_{out}	kW	70.9	59.5

It should be noted that a saliency ratio of the inset type of the IPM motor could be higher with distributed armature winding, which has less leakage reactance, which reduces the difference between q- and d-axes synchronous reactances [7]. However, the considered machines with distributed winding (Fig. 3 (a)) can not completely satisfy the design requirements. In the following section explanations of this are given.

IV. DISTRIBUTED OR CONCENTRATED ARMATURE WINDING

A. *End winding overhang*

Lap distributed windings have long end winding overhangs which significantly increase the axial length of the machine. However, the end windings could be compressed up to the same overhang length as in the concentrated winding. The possibility to compress the armature coils, which have the limit flexibility of the insulation and the copper wires, can be checked only by experiments on real-world windings. Without those experiments it is difficult to define that the DW motor satisfies design requirements specifically in total motor length.

B. *Comparison of the SPM machine performances with distributed and concentrated armature windings*

In order to compare the distributed winding (DW) and concentrated winding (CW) motors performance at base speed and CPSR the three machines with DW have been designed by using only developed analytical method (section IV from the Part I of this paper). The rotors of all designs are SPM rotors but with different dimensions of the magnets and back-iron. Armature windings of the DW machines are conventional full-pitched distributed windings with the following parameters: q=1, m_1=3, Z=24, p=4. The motor geometries are shown in Fig. 9. These DW motors are compared with the designed SPM CW machine, which data is given in section V from the Part I of this paper.

The first DW design, DW1, is constrained to have the same outer diameter and magnet height; the second motor, DW2, has the same airgap diameter and also the same magnet height. The third DW machine, DW3, is designed to have the same outer diameter and near the same FW operation.

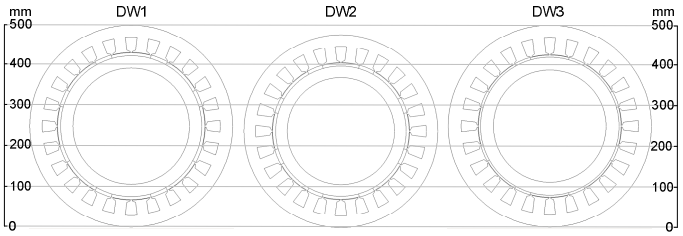

Fig. 9: Cross-sections of the geometries of the studied PM motors with distributed windings

TABLE IV
COMPARISON CONSTRAINTS

Description	Symbol	Value	Unit
Output power at base speed	P_{out}	69	kW
Number of pole pairs	p	4	-
Phase voltage (rms)	V_1	≤ 220	V
Magnet span angle	α_m	132, 126*	el.deg.
Armature current density (rms)	J_1	5	A/mm^2
Airgap height	δ	1	mm
Motor active length	l_1	100	mm
Motor total length	l_{tot}	204	mm
Base speed	n_1	800	rpm
Magnet remanence	B_r	1.175	T
Magnet relative recoil permeability	μ_r	1.05	-
Stator and rotor back-iron flux densities	B_{ys}, B_{yr}	1.65	T
Stator tooth peak flux density	B_{zm}	≤ 1.84	T
Net slot fill factor	k_f	0.5	-

* - the magnet span angle of 126^o is selected for the distributed winding machines to reduce per unit back-emf and, therefore, to improve FW operation. The further reduction of the magnet span angle could cause significant increasing the cogging torque and finally is not appropriate.

All designed DW machines have been constrained to have the data, which is presented in Table IV. One of the main constraints is an output power at the base speed, which is also fixed. This has allowed making the comparison of the electrical loadings of the machines at the most loaded operation point in terms of armature current and highest flux densities in the motor iron. The last circumstance is described under conditions that the armature reaction flux is oriented along *q*-axis and the demagnetization effect is minimum. The stack length and total motor length are also comparison constraints. The end winding overhangs of the DW machines are shortened by introducing compressions coefficients, k_{comp}, which are ratios between the overhangs of the corresponding DW and CW machine.

Armature current densities and the copper slot fill factors have been also fixed. The net slot fill factor, k_f, of the DW machines could not be higher of 0.5, which is less than the net slot fill factor k_f =0.65 of the designed CW machine (Table I in the Part I of this paper). In order to limit a number of possible stator core dimensions and to keep steel saturation at the same level, as in the CW machine, the flux densities in the back-iron and stator teeth have been constrained to 1.65 T and 1.84 T, respectively.

Table V summarizes the basic geometry, winding and performance data of the studied three DW motors and the CW motor. The normalized power versus speed envelopes of the studied machines is shown in Fig. 10. The output power has been normalized by using apparent power *S*, which is different for the all four machines. The DW1 and DW2 machines, having the same magnet height as in the CW machine, have higher power factors at low speeds and, therefore, are more efficient considering inverter capacity. It could be explained by that these motors have lower leakage reactance (Table V). However, these DW machine designs are not capable to operate in the wide CPSR, since the back-emfs, E_0, are significantly higher of the corresponding *d*-axis armature reactances, X^*_d, and ratios E_0/X^*_d notably higher than the unity.

TABLE V
COMPARISON OF THE THREE VARIANTS OF THE DW MOTORS AND DESIGNED CW MOTOR

Description	Symbol	DW1	DW2	DW3	CW
Stator outer diameter, mm	D_{OD}	500	477	499	501.3
Average airgap diameter, mm	D_{1av}	364	337	351	337
Magnet height, mm	h_m	7.5	7.5	5	7.5
Electrical loading (rms), A/m	A_1	48000	56200	54500	56000
Phase voltage (rms), V	V_1	205.8	218	215.4	219.5
Phase current (rms), A	I_1	127.4	124.3	139.5	138.3
Number of series turns per phase	w_1	72	80	72	78
End winding compression coefficient	k_{comp}	0.53	0.558	0.54	-
Apparent power, kVA	S	78.8	81.2	90.1	91.1
Power factor at base speed	$cos\varphi$	0.876	0.85	0.766	0.757
Back-emf, p.u.	E_0	0.847	0.821	0.739	0.741
d-axis synchronous reactance, p.u.	X^*_d	0.483	0.527	0.643	0.653
Armature leakage reactance, p.u.	X^*_σ	0.18	0.208	0.212	0.424
Ratio of the E_0 and X^*_d	E_0/X^*_d	1.75	1.56	1.15	1.13
Armature copper weight, kg	W_{Cu}	35	36.5	37.7	22.8
Lamination weight, kg	$W_{sl}+W_{rl}$	78.2	72.7	83.6	83.2
Magnets weight, kg	W_{rm}	4.6	4.2	2.9	4.4
Risk of the magnet demagnetization at symmetrical 3-phase short circuit	-	Yes	Yes	Yes	No

All four studied motors are finite speed machines, since their ratios E_0/X^*_d are larger than the unity [1]. The better FW operation of a PM motor corresponds with lower values of the E_0/X^*_d, and at $E_0/X^*_d < 1$ machine becomes the infinite speed machine, that virtually is ideal for the CPSR. In a DW machine it could be achieved by reducing the magnet height, which is limited by increasing the armature reaction flux and, therefore, could lead to the PM demagnetization. For the considered DW machines it has been investigated that even at the height of 7.5 mm the magnets are assessed to be

demagnetized at symmetrical three phase short circuit, which could happen at the motor terminals. This is one of the main disadvantages of such machine type. The designed CW machine also has the same magnet height but the demagnetization effect of the armature reaction flux is significantly reduced by the notably higher armature leakage reactance (Table V), which limits the current at short circuit conditions.

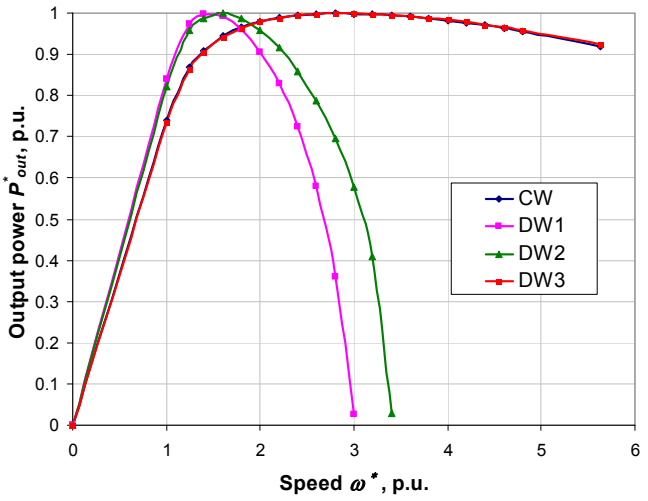

Fig. 10: Normalized output power versus speed characteristics of the considered motors

For the DW3 and CW motors the output power versus speed characteristics are almost matched that could be explained by that ratio of the E_0 and X^*_d is practically the same for both machines. In the DW3 machine the high value of the X^*_d and the low value of the E_0 are reached by reducing the PM height from 7.5 mm up to 5 mm. In accordance with the performance given in Fig. 10, the DW3 machine could be an alternative to the CW motor.

The DW1 motor design has the lowest value of the electrical loading, due to the largest airgap diameter of this machine (Table V). In spite of that the FW operation of the DW1 motor is the worst among the other machines. Since the output power at base speed and active length of the considered machines are fixed, the electrical loading is defined almost only by the airgap diameter (neglecting the differences in the airgap flux at open circuit conditions), as given in (3).

The weights of the motors' active parts are presented in Fig. 11 and in Table V as well. Weights of laminations for the all four machine designs differ in accordance with total airgap flux and dimensions of the stator and rotor cores. The DW2 motor, having almost the same electrical loading as in the CW machine, has the lowest stator outer diameter and lowest laminations' weight. The main reason is that in the considered DW there are no subharmonics in armature reaction flux, which in addition to the fundamental harmonic magnetize the CW machine, and the dimensions of the laminations have been decreased.

The DW3 machine has the largest fundamental harmonic of the armature flux, as it is mentioned before, due to lowest magnet height, and that is why laminations' weight is the largest among others DW machine designs (Table V). But the magnet weight in that machine is correspondingly the lowest.

The armature copper weight of the DW machines is notably higher than in the CW machine because of longer end windings. From Table V the difference between copper weights of the DW and CW machines is about of 14 kg. This quite big difference makes the CW motor the lightest machine among considered variants.

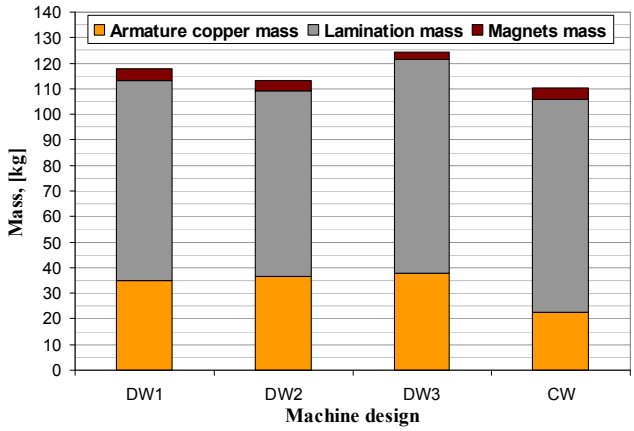

Fig. 11: Normalized output power versus speed characteristics of the considered motors

Summarizing the comparison of the DW and CW machines, which has been provided in this section, it could be concluded the following:

1) The SPM motor with the lap DW could be designed with wide CPSR by selecting the lower magnet heights and, therefore, lower magnet volumes;
2) Due to the high electrical loading and, therefore, high armature reaction flux the PMs in the DW machine are demagnetized at possible three phase symmetrical short circuit at the motor terminals (Table V). The additional measures should be implemented in the drive in order to avoid the failure mode;
3) Since the axial length of the designing PM motor is significantly limited by the design requirements, and the required compression coefficient, k_{comp} = 0.53, looks unrealizable (at least the opposite fact is not checked by the experiment yet), the DW machine is not considered as a possible candidate for the given application.

The possibility of using the IPM motor with the DW has not been studied separately. However, it is declared that this motor configuration has the disadvantages analogous to the IPM CW machine (section II) and the SPM DW machine (section III). Even since the saliency ratio of the IPM DW motor is higher than in the IPM CW motor, the main design limitation of the DW machine is a remaining problem with the long end winding overhangs.

V. CONCLUSION

A main contribution of this paper is the comparative (qualitative and quantitative) study of the different "in-wheel" motor configurations for the hybrid electric drive application. This research has been completed based on the developed semi-analytical tools. The tough design requirements as the very limited volume envelope, high output power, wide CPSR and pre-selected indirect cooling system lead to constraint variants of the possible motor type.

After completion of the extended comparative analysis the designed surface-mounted PM motor with the concentrated armature winding is selected as the most suitable design for the specified application.

REFERENCES

[1] W. Soong and T. J. E. Miller, "Field weakening performance of brushless synchronous AC motor drives," Proc. IEE—Elect. Power Appl., vol. 141, no. 6, pp. 331–340, Nov. 1994.

[2] EL-Refaie, A. M., T. M. Jahns, "Comparison of Synchronous PM Machine Types for Wide Constant-Power Speed Range Operation", 2005 IEEE Industry Applications Society Annual Meeting, 2-6 October 2005, Hong Kong.

[3] A.V. Ivanov-Smolenskii.: *Electrical machines*, Energoatomizdat, Moscow, 1980. (in Russian)

[4] A.I. Borisenko, *Aerodynamics and heat transfer in electrical machines*, Energia, Moscow, 1974 (in Russian)

[5] J.R. Hendershot Jr. and T.J.E. Miller, *Design of brushless permanent magnet motors*,. Oxford, U.K.: Clarendon, 1994.

[6] Morimoto S., Takeda Y., Hirasa T., and Taniguchi K.: "Expansion of operating limits for permanent magnet motor by optimum flux-weakening", Industry Applications Society Annual Meeting, 1989., Conference Record of the 1989 IEEE, 1-5 Oct. 1989 Page(s):51 - 56 vol.1

[7] EL-Refaie, A. M., T. M. Jahns: "Comparison of Synchronous PM Machine Types for Wide Constant-Power Speed Range Operation", 2005 IEEE Industry Applications Society Annual Meeting, 2-6 October 2005, Hong Kong